Riemannian Wavefield Extrapolation: Non-orthogonal coordinate systems

Jeff Shragge

(October 10, 2007)

Running head:

ABSTRACT

Riemanninan wavefield extrapolation (RWE) is used to model one-way wave propagation on generalized coordinate meshes. Previous RWE implementations assume that coordinate systems are defined by either orthogonal or semi-orthogonal geometry. This restriction leads to situations where coordinate meshes suffer from problematic bunching and singularities. In this paper, I develop a procedure to avoid many of these problems by posing wavefield extrapolation on smooth, but generally non-orthogonal and singularity-free, coordinate meshes. The resulting extrapolation operators include additional terms that describe non-orthogonal propagation. These extra degrees of complexity, however, are offset by smoother coefficients that are more accurately implemented in one-way extrapolation operators. I validate my theory of non-orthogonal propagation with two analytic coordinate system examples, and I present a method for eliminating any remaining singularities from coordinate systems. I demonstrate non-orthogonal RWE by numerical calculation of 2D and 3D Green's functions for cylindrical and near-spherical geometry. Results from 2-D benchmark testing suggest that the computational overhead associated with the RWE approach is roughly 35% greater than Cartesian-based extrapolation.

INTRODUCTION

A persistent goal of wave-equation migration research is to improve seismic imaging capabilities in complex geologic settings. Although ubiquitous velocity model uncertainty and uneven illumination can contribute greatly to image interpretation ambiguity in these contexts, extrapolation operator inaccuracy remains a significant problem. The central issues with conventional one-way wave-equation extrapolation operators are well documented: while naturally handling wavefield multipathing in the presence of lateral velocity variation, they are of limited accuracy at large propagation angles and cannot propagate turning waves by design (though extensions including phase-shift table lookup (Hale et al., 1992) or two-pass migration (Zhang et al., 2006) address some of these concerns). Propagation errors are subsequently manifest in migration images as defocused or misplaced reflectors or even by a complete absence of interpretable reflectivity. Accordingly, minimizing these deleterious effects should improve image quality and any subsequent interpretation based thereon.

One strategy for reducing extrapolation operator inaccuracy is to decompose the complete computational grid into subdomains oriented in the wave propagation direction. Examples of this approach include Gaussian beams (Hill, 2001), beam-waves (Brandsberg-Dahl and Etgen, 2003), coherent states (Albertin et al., 2001) or tilted Cartesian meshes (Etgen, 2002). The key concept in each of these approaches is that a judicious choice of reference frame lowers the effective local propagation angle, reducing the need for expensive global extrapolation operators and enabling imaging of turning waves. Sava and Fomel (2005) followed this approach in developing Riemannian wavefield extrapolation (RWE), a theory of one-way wavefield propagation for 3D numerically generated, semi-orthogonal meshes. This

formulation specifies the wave-equation operators appropriate for wavefield extrapolation on generalized computational meshes. One important ramification is that the user is free to specify the degree to which wave-propagation direction is aligned with the computational mesh. However, finding the optimal trade-off between computational mesh simplicity, how well the mesh conforms to the wavefield propagation direction, and the computational cost is not a straightforward task.

RWE was initially implemented to model high-quality Green's functions (Sava and Fomel, 2005). This process involved extrapolating wavefields on a point-source coordinate mesh comprised of a suite of rays traced beforehand through a smoothed version of the migration velocity model. Hence, RWE computational meshes explicitly were asserted to exhibit ray-field characteristics: semi-orthogonal geometry with an extrapolation direction (i.e. travel-time along a ray) orthogonal to the two other axes (i.e. shooting angles) that are not necessarily mutually orthogonal. This geometric restriction leads to wave-equation dispersion relationships that contain a number of mixed spatial and wavenumber domain terms (i.e. a simultaneous dependence on $\mathbf{x}$ and $\mathbf{k}$) that encode coordinate system geometry. In most examples, modeled Green's function estimates interpolated into the Cartesian domain are highly accurate at large propagation angles; however, accuracy is compromised in certain situations exhibiting unfavorable characteristics such as extensive mesh compression/extension or in the presence of singularities.

Semi-orthogonal geometry, though, can be an overly restrictive assertion. One problematic example is the coordinate system singularities observed in Figure 1a. These situations arise wherever a mesh is generated from a rayfield that includes a crossing set of rays, which generates spatial singularities and singular Jacobians that lead to zero-division during wavefield extrapolation. Although ray-coordinate singularities can be avoided by iterative veloc-

ity model smoothing, this less-than-ideal solution counters the goal of having a coordinate system conformal to the wavefield propagation direction. A second example of restrictive semi-orthogonal geometry is illustrated in Shragge and Sava (2005), who formulate a wave-equation migration from topography strategy that poses wavefield extrapolation directly in locally orthogonal meshes conformal to the acquisition surface (see Figure 1b). This approach successfully generates subsurface images beneath areas exhibiting longer wavelength and lower amplitude relief; however, imaging results in situations involving more rugged acquisition topography degrade due to the grid compression/extension demanded by semi-orthogonality geometry of).

In this paper, I argue that generalizing RWE to non-orthogonal geometries resolves the issues associated with semi-orthogonal meshes, and affords the use of smoother computational meshes and a procedure for removing all coordinate singularities. Non-orthogonal propagation results in an extrapolation wavenumber that consists of two additional mixed-domain terms relative to the wavenumber associated with semi-orthogonal RWE. I then use this wavenumber to implement a one-way extrapolation operator in the usual sense of wave-equation imaging.

A goal of this paper is to develop and implement a one-way wave-equation extrapolation operator appropriate for RWE in 3D non-orthogonal coordinates. A second goal is to specify a procedure for generating unconditionally singularity-free computational meshes. My development follows that of Sava and Fomel (2005); however, I recast the theory in a more compact notation for a closer analytic connection of the generalized computation geometry with the underlying Cartesian grid. The paper begins with the formulation of the 3D Riemannian acoustic wave-equation and the corresponding non-orthogonal one-way wavefield extrapolation wavenumber. Appendix A presents an overview of the required

differential geometry theory, while the split-step Fourier extrapolation operator used in the examples is derived in Appendix B. Two analytic 2D non-orthogonal coordinate system examples are then provided to validate the theory. The final sections detail a procedure for generating singularity-free coordinate systems, present 2D and 3D Green's functions estimates modeled in cylindrical and near-spherical coordinates, respectively, and I discuss the relative computational cost and memory overhead of the RWE method.

ACOUSTIC WAVE EQUATION IN 3D GENERALIZED RIEMANNIAN SPACES

To specify the acoustic wave-equation in a 3D Riemannian space, we must formulate the physics of wave-propagation in a generalized coordinate system framework. By definition, generalized Riemannian coordinates are related to the underlying Cartesian mesh by unique transformations (i.e. singularity-free and one-to-one). In this paper, I use a notation where a generalized coordinate system $\xi = \{\xi_1, \xi_2, \xi_3\}$ is mapped to a Cartesian grid $\mathbf{x} = \{x_1, x_2, x_3\}$ through transformation $\xi_i(x_j) = f_i$. Provided these conditions are met, the monochromatic wave-equation for an acoustic wavefield, U, in a generalized Riemannian space is,

$$\nabla_\xi^2 U = -\omega^2 s_\xi^2 U, \tag{1}$$

where ∇_ξ^2 is the Laplacian operator applied in coordinates ξ, ω is frequency, and s_ξ is the propagation slowness.

A correct formulation of the wave-equation in coordinate system ξ requires that Laplacian operator ∇_ξ^2 be specified by differential geometry relationships. (An overview of necessary differential geometry theory is provided in Appendix A.) The Laplacian operator in

generalized coordinates is (Synge and Schild, 1949),

$$\nabla^2_\xi U = \frac{1}{\sqrt{|\mathbf{g}|}} \frac{\partial}{\partial \xi_i} \left(\sqrt{|\mathbf{g}|} g^{ij} \frac{\partial U}{\partial \xi_j} \right) = \frac{1}{\sqrt{|\mathbf{g}|}} \frac{\partial}{\partial \xi_i} \left(m^{ij} \frac{\partial U}{\partial \xi_j} \right), \quad i,j = 1,2,3, \tag{2}$$

where g^{ij} is an element of the metric tensor $\mathbf{g}$, $|\mathbf{g}|$ is the metric tensor discriminant, and $m^{ij} = \sqrt{|\mathbf{g}|} g^{ij}$ is weighted metric tensor element that enables a more compact notation. Unless otherwise stated, summation over all repeated indicies (i.e. $i,j = 1,2,3$) is assumed throughout this paper. Substituting equation 2 into 1 leads to the Helmholtz equation appropriate for propagating waves through a 3D Riemannian space (Sava and Fomel, 2005),

$$\frac{1}{\sqrt{|\mathbf{g}|}} \frac{\partial}{\partial \xi_i} \left(m^{ij} \frac{\partial U}{\partial \xi_j} \right) = -\omega^2 s^2 U. \tag{3}$$

The first step in developing a generalized RWE wave-equation dispersion relationship is to expand the derivative terms in equation 3 and multiply through by $\sqrt{|\mathbf{g}|}$ to obtain,

$$\frac{\partial m^{ij}}{\partial \xi_i} \frac{\partial U}{\partial \xi_j} + m^{ij} \frac{\partial^2 U}{\partial \xi_i \partial \xi_j} = -\sqrt{|\mathbf{g}|} \omega^2 s^2 U. \tag{4}$$

The derivation of the 3D RWE acoustic wave equation deviates here from that found in Sava and Fomel (2005), who represent the metric tensor with only four independent coefficients. The remaining two independent coefficients are explicitly set to zero in order to satisfy the semi-orthogonal geometry restriction. In this development, I follow a more general approach that representsss the metric tensor with the full six independent coefficients. This is the key extension developed in this paper that leads to the greater flexibility in coordinate system design discussed below.

The spatial derivative of the weighted metric tensor in the first term of equation 4 is written concisely using the following substitution,

$$n^j = \frac{\partial m^{ij}}{\partial \xi_i} = \frac{\partial m^{1j}}{\partial \xi_1} + \frac{\partial m^{2j}}{\partial \xi_2} + \frac{\partial m^{3j}}{\partial \xi_3}. \tag{5}$$

Fields n^j are interpreted as measures of the rates by which space expands, compresses and/or shears in the j^{th} direction and can be non-zero even for orthogonal coordinate systems. Using this substitution, equation 4 is rewritten,

$$n^j \frac{\partial U}{\partial \xi_j} + m^{ij} \frac{\partial^2 U}{\partial \xi_i \partial \xi_j} = -\sqrt{|\mathbf{g}|}\omega^2 s^2 U. \tag{6}$$

A wave-equation dispersion relation is developed by replacing the partial differential operators acting on wavefield U with their Fourier domain wavenumber duals (Claerbout, 1985),

$$\left(m^{ij} k_{\xi_i} - \mathrm{i} n^j\right) k_{\xi_j} = \sqrt{|\mathbf{g}|}\omega^2 s^2, \tag{7}$$

where $\mathrm{i}k_{\xi_i}$ is the Fourier domain dual of differential operator $\frac{\partial}{\partial \xi_i}$. Note that the use of these dual operators is strictly accurate only for the case of constant coefficients. Situations where $s, m^{ij}, |\mathbf{g}|$ or n^j spatially vary leads to a simultaneous spatial and Fourier wavenumber dependence. However, I handle this through various approximations discussed below.

Equation 7 represents the dispersion relationship required to propagate a wavefield through a generalized 3D Riemannian space. Quantity m^{ij} in the first term, $m^{ij} k_{\xi_i} k_{\xi_j}$, is a measure of the dot product between wavenumber vectors in the k_{ξ_i} and k_{ξ_j} directions (i.e. orthogonal wavenumbers will have coefficients $m^{ij} = 0$ for $i \neq j$). Fields n^j in the second term, $\mathrm{i}n^j k_{\xi_j}$, represent a scaling of wavenumber k_{ξ_j} caused by local expansion, contraction and/or shearing of the coordinate system in the j^{th} direction.

Note that the expression in equation 7 reduces to the more familiar Cartesian expression when introducing $n^j = 0$ and $m^{ij} = \delta^{ij}$:

$$k_{\xi_i} k_{\xi_i} = k_{\xi_1}^2 + k_{\xi_2}^2 + k_{\xi_3}^2 = \omega^2 s^2. \tag{8}$$

Extrapolation wavenumber isolation

Specifying a one-way extrapolation operator requires isolating one of the wavenumbers in equation 7. In this paper, I associate the extrapolation direction with coordinate ξ_3. Expanding equation 7 by an evaluation of indices and rearranging the result yields,

$$m^{33}k_{\xi_3}^2+\left(2m^{13}k_{\xi_1}+2m^{23}k_{\xi_2}-\mathrm{i}\,n^3\right)k_{\xi_3}=\sqrt{|\mathbf{g}|}\omega^2 s^2+\mathrm{i}\left(n^1k_{\xi_1}+n^2k_{\xi_2}\right)-m^{11}k_{\xi_1}^2-m^{22}k_{\xi_2}^2-2m^{12}k_{\xi_1}k_{\xi_2}. \tag{9}$$

Wavenumber k_{ξ_3} is then isolated through a complete-the-square transform

$$k_{\xi_3}=-a_1k_{\xi_1}-a_2k_{\xi_2}+\mathrm{i}a_3\pm\left[a_4^2\omega^2-a_5^2k_{\xi_1}^2-a_6^2k_{\xi_2}^2-a_7k_{\xi_1}k_{\xi_2}+\mathrm{i}a_8\,k_{\xi_1}+\mathrm{i}a_9\,k_{\xi_2}-a_{10}^2\right]^{\frac{1}{2}}, \tag{10}$$

where the non-stationary coefficients of a_i in equation 10 are presented in the following vector $\mathbf{a}$,

$$\mathbf{a}=\left[\frac{g^{13}}{g^{33}}\quad\frac{g^{23}}{g^{33}}\quad\frac{n^3}{2m^{33}}\quad\frac{s}{\sqrt{g^{33}}}\quad\sqrt{\frac{g^{11}}{g^{33}}-\left(\frac{g^{13}}{g^{33}}\right)^2}\quad\sqrt{\frac{g^{22}}{g^{33}}-\left(\frac{g^{23}}{g^{33}}\right)^2}\quad\ldots\right.$$
$$\left.\ldots\left[\frac{2\,g^{12}}{g^{33}}-\frac{2\,g^{13}\,g^{23}}{(g^{33})^2}\right]\quad\left[\frac{n^1}{m^{33}}-\frac{m^{13}\,n^3}{(m^{33})^2}\right]\quad\left[\frac{n^2}{m^{33}}-\frac{m^{23}\,n^3}{(m^{33})^2}\right]\quad\frac{n^3}{2m^{33}}\right]^{\mathbf{T}}. \tag{11}$$

ss Note that the coefficients contain mixed m^{ij} ssand g^{ij} terms and globally positive terms a_4, a_5, a_6 and a_{10} are squared.

The special Cartesian case is again recovered from the two equations above by substituting $n^j=0$ and $g^{ij}=\delta^{ij}$ for the coefficients of equation 11

$$k_{\xi_3}=\left[s^2\omega^2-k_{\xi_1}^2-k_{\xi_2}^2\right]^{\frac{1}{2}}. \tag{12}$$

The dispersion relationship specified by equations 10 and 11 contains ten coefficients that represent mixed-domain fields. Similar to Cartesian-based wavefield extrapolation through homogeneous media, a constant-coefficient Fourier-domain $(\omega-\mathbf{k}_\xi)$ phase-shift

extrapolation scheme can be developed to recursively advance a wavefield from level ξ_3 to level $\xi_3 + \Delta\xi_3$ (Gazdag, 1978),

$$U(\xi_3 + \Delta\xi_3, k_{\xi_1}, k_{\xi_2}; \omega) = U(\xi_3, k_{\xi_1}, k_{\xi_2}; \omega) \mathrm{e}^{\mathrm{i}k_{\xi_3}\Delta\xi_3}. \tag{13}$$

If U represents a post-stack wavefield, an image I can be produced from the propagated wavefield through an imaging condition (Claerbout, 1985),

$$I(\xi_3, \xi_1, \xi_2) = \sum_{\omega} U(\xi_3, \xi_1, \xi_2; \omega). \tag{14}$$

Situations where coefficients vary across an extrapolation step, though, require further approximations. One straightforward approach is a multi-coefficient split-step Fourier (SSF) method (Stoffa et al., 1990; Sava and Fomel, 2005). This method uses Taylor expansions of the dispersion relation about a set of reference parameters to form a bulk phase-shift operator in the Fourier domain ($\omega - \mathbf{k}_\xi$). Differences between the reference and true parameters then form a correction term applied in the mixed $\omega - \xi$ domain. For non-orthogonal coordinate systems described by equations 10 and 11, I modify the SSF approach of Sava and Fomel (2005) as detailed in Appendix B.

The accuracy of the multi-coefficient SSF approach is directly related to the degree to which coefficients in equation 11 vary at each propagation step. At a first glance, one might expect that far too many expansions are required to make a PSPI approach practical. (For example, three reference expansions for each of the ten terms would seemingly require $3^{10} = 59049$ separate wavefield extrapolations.) However, three factors combine to greatly reduce the total number of required reference coefficient sets.

First, the a_i coefficients in equation 10 are highly correlated because they are composed of similar metric tensor elements g^{ij}. Thus, the central issue is how accurately can we

characterize vector coefficient fields. Fortunately, this problem is similar to the quantization problem in computer graphics: What is the fewest number of colors by which an image can be represented given a maximum allowable error? To address this issue, I calculate reference coefficients using a multi-dimensional Lloyd's algorithm developed by Tang and Clapp (2006). This iterative procedure represents the multi-dimensional histogram of the coefficients with the sparsest number of points within a specified error tolerance. For further information and examples the reader is directed to Tang and Clapp (2006).

Second, numerous situations exists where some coefficients are zero or negligible. For example, the mixed-domain fields for a 3D weakly non-orthogonal coordinate system within a kinematic approximation (i.e. zeroed imaginary terms) is accurately approximated with four coefficients. In practice, I use the following relationship to determine where non-orthogonal coefficients may be zeroed at any extrapolation step:

$$\hat{g}^{ij} = \begin{cases} 0, & g^{ij} < 0.01 \left|\min\{g^{11}, g^{22}, g^{33}\}\right| \\ g^{ij} & \text{otherwise} \end{cases} \tag{15}$$

where the circumflex accent $\hat{g}^{ij}$ denotes approximation. Appendix C details situations where additional approximations are appropriate. Third, one may apply algorithms that locally smooth the coordinate system mesh, which reduces the spatial variability of the coefficients and allows a more reliable representation of wavenumber k_{ξ_3}.

NUMERICAL MODELING EXAMPLES

This section presents numerical modeling examples that help validate the non-orthogonal RWE theory. I begin with the two basic 2D analytic examples of sheared Cartesian and polar ellipsoidal coordinates. I then present a method for generating singularity-free coordinate meshes and illustrate this approach with 2D and 3D Green's function modeling.

2D sheared Cartesian coordinate system

An instructive analytic coordinate system to examine is a 2D sheared Cartesian grid formed by a uniform sssshearing action on a 2D Cartesian mesh (see Figure 2a). This coordinate system is uniquely specified by one additional degree of freedom and is related to an underlying Cartesian mesh through the following transformation,

$$\begin{bmatrix} x_1 \\ x_3 \end{bmatrix} = \begin{bmatrix} 1 & \cos\theta \\ 0 & \sin\theta \end{bmatrix} \begin{bmatrix} \xi_1 \\ \xi_3 \end{bmatrix}, \tag{16}$$

where θ is the shear angle of the coordinate system ($\theta = 90°$ is Cartesian). The metric tensor of this transformation is,

$$[g_{ij}] = \begin{bmatrix} \frac{\partial x_k}{\partial \xi_1}\frac{\partial x_k}{\partial \xi_1} & \frac{\partial x_k}{\partial \xi_1}\frac{\partial x_k}{\partial \xi_3} \\ \frac{\partial x_k}{\partial \xi_1}\frac{\partial x_k}{\partial \xi_3} & \frac{\partial x_k}{\partial \xi_3}\frac{\partial x_k}{\partial \xi_3} \end{bmatrix} = \begin{bmatrix} g_{11} & g_{13} \\ g_{13} & g_{33} \end{bmatrix} = \begin{bmatrix} 1 & \cos\theta \\ \cos\theta & 1 \end{bmatrix}, \tag{17}$$

and has a discriminant $|\mathbf{g}| = \sin^2\theta$ and an associated metric tensor g^{ij} given by,

$$\left[g^{ij}\right] = \frac{1}{\sin^2\theta} \begin{bmatrix} 1 & -\cos\theta \\ -\cos\theta & 1 \end{bmatrix}. \tag{18}$$

Note that because the tensor in equation 18 is coordinate invariant, equation 6 simplifies to,

$$\nabla^2_\xi U = g^{ij} \frac{\partial^2 U}{\partial \xi_i \partial \xi_j} = -\omega^2 s^2 U, \tag{19}$$

which generates the following dispersion relation,

$$g^{ij} k_{\xi_i} k_{\xi_j} = \omega^2 s^2. \tag{20}$$

Expanding out these terms leads to an expression for wavenumber k_{ξ_3},

$$k_{\xi_3} = -\frac{g^{13}}{g^{33}} k_{\xi_1} \pm \sqrt{\frac{s^2\omega^2}{g^{33}} - \left(\frac{g^{11}}{g^{33}} - \left(\frac{g^{13}}{g^{33}}\right)^2\right) k^2_{\xi_1}}. \tag{21}$$

Substituting the values of the associated metric tensor in equation 18 into equation 21 yields,

$$k_{\xi_3} = \cos\theta \; \mathrm{k}_{\xi_1} \pm \sin\theta \sqrt{\mathrm{s}^2\omega^2 - \mathrm{k}_{\xi_1}^2}, \tag{22}$$

which is appropriate for performing RWE on the 2D sheared Cartesian coordinate system shown in Figure 2a.

Figure 2b shows the results of extrapolating plane waves in a Cartesian coordinate system sheared 25° from vertical. The background velocity model is 1500 m/s and the zero-offset data consist of 4 flat plane-waves at times $t = 0.2, 0.4, 0.6$ and 0.8 s. Zero-offset migration results generated by equation 14 show migrated reflectors at the expected depths of z=300, 600, 900, and 1200 m. The propagation creates explainable boundary artifacts. Those on the left are caused by the common edge effect of waves reflecting off the boundary at non-normal incidence. Hyperbolic diffractions on the right arise from propagating truncated plane waves and are independent of the coordinate system. Mitigating these types of artifacts is not difficult, though, because existing techniques in Cartesian wavefield extrapolation craft still apply (e.g. cosine boundary tapers).

Polar Ellipsoidal Coordinates

A second example is an ellipsoidal polar coordinate system (see Figure 3a) appropriate for turning wave migration. A polar ellipsoidal coordinate system is specified by,

$$\begin{bmatrix} x_1 \\ \\ x_3 \end{bmatrix} = \begin{bmatrix} a(\xi_3)\,\xi_1 \cos\xi_3 \\ \\ a(\xi_3)\,\xi_1 \sin\xi_3 \end{bmatrix}, \tag{23}$$

where coordinate ξ_1 is the radius from the center focus, ξ_3 is polar angle, and $a = a(\xi_3)$ is a smooth function controling coordinate system ellipticity that has curvature parameters

$b = \frac{\partial a}{\partial \xi_3}$ and $c = \frac{\partial^2 a}{\partial \xi_3^2}$. The metric tensor g_{ij} for the polar ellipsoidal coordinate system defined in equation 23 is,

$$[g_{ij}] = \begin{bmatrix} a^2 & \xi_1\, a\, b \\ \xi_1\, a\, b & \xi_1^2(b^2 + a^2) \end{bmatrix}, \tag{24}$$

and has a metric discriminant given by $|\mathbf{g}| = a^4 \xi_1^2$. The associated and weighted associated metric tensors are given by,

$$\left[g^{ij}\right] = \begin{bmatrix} \frac{b^2+a^2}{a^4} & -\frac{b}{a^3\,\xi_1} \\ -\frac{b}{a^3\,\xi_1} & \frac{1}{a^2\,\xi_1^2} \end{bmatrix} \quad \text{and} \quad \left[m^{ij}\right] = \begin{bmatrix} \frac{\xi_1(b^2+a^2)}{a^2} & -\frac{b}{a} \\ -\frac{b}{a} & \frac{1}{\xi_1} \end{bmatrix}. \tag{25}$$

Tensors g^{ij} and m^{ij} are used to form the extrapolation wavenumber appropriate for one-way wavefield propagation on a 2D polar ellipsoidal mesh. However, because the computational mesh is non-stationary, we must also compute the n^i fields: $n^1 = \frac{a^2+2b^2-ac}{a^2}$ and $n^3 = 0$. Inserting these values leads to the following extrapolation wavenumber expression (see equations C-7 and C-8),

$$k_{\xi_3} = \frac{\xi_1 b}{a} k_{\xi_1} \pm \sqrt{a^2\xi_1^2 s^2\omega^2 - \xi_1^2 k_{\xi_1}^2 - \mathrm{i}k_{\xi_1}\xi_1\left(\frac{a^2+2b^2-ac}{a^2}\right)}. \tag{26}$$

The kinematic approximation of equation 26 (see equations C-9 and C-10) is given by,

$$\hat{k_{\xi_3}} = \xi_1 \left[\frac{b}{a} k_{\xi_1} \pm \sqrt{a^2 s^2\omega^2 - k_{\xi_1}^2}\right], \tag{27}$$

and further restricting to the orthogonal polar case where $a = 1$ and $b = 0$ (see equations C-13 and C-14) yields,

$$\hat{k_{\xi_3}} = \pm\xi_1\sqrt{s^2\omega^2 - k_{\xi_1}^2}, \tag{28}$$

which is examined in Nichols (1994).

Figure 3 shows a wavefield extrapolation example for an ellipsoidal polar coordinate system in equation 23 defined by ellipticity parameter $a(\xi_3) = 1 + 0.2\,\xi_3 - 0.05\,\xi_3^2$. The upper and lower panels of Figure 3 correspond to velocity/coordinate and wavefield domains,

respectively. Similarly, the left and right panels represent the Cartesian and Riemannian domains. Note that wavefield interpolation between the latter two domains is possible because of the established mapping relationships. Figure 3a shows the polar ellipsoidal coordinate system mesh overlying a linear $v(z) = 1500 + 0.35\,z$ m/s velocity function. Figure 3b presents the velocity model mapped into the RWE domain under the transformations defined in equation 23. The test data consist of ten plane waves defined on the surface between 1000 m and 9000 m by ray parameter $p_x = -0.5$ s/km. After propagation to greater depths, the waves are no longer planar and pass through a turning point before moving upward to the left (Figure 3c and 3d). The wave tops, though, travel through slower material and have not yet overturned. One observation is that if propagating wavepaths can be well represented by a single ellipticity parameter $a = a(\xi_3)$, then a polar elliptical mesh could form the coordinate basis for a plane-wave migration strategy that is potentially more dynamic than tilted Cartesian coordinates.

GENERATING SINGULARITY-FREE COORDINATE MESHES

A computational mesh design challenge is finding a RWE coordinate system that is fairly conformal to the wavefield propagation direction yet unconditionally singularity-free. Figure 4a shows a v(z) velocity model with three Gaussian anomaly inclusions overlain by a ray-coordinate system calculated by Huygens' ray-front tracing (Sava and Fomel, 2001). Note that the anomalies cause both mesh singularities to the left and right of the model as well as a grid rarefaction directly beneath the shot-point.

Figure 4b shows the single-valued isochrons of the first-arrival Eikonal equation solution for the same shot-point presented in the top panel. Note that isochrons generally conform to the propagation direction and can be used to construct the extrapolation steps of a RWE

computational mesh. The first step in the mesh generation procedure is to extract the initial and final isochron surfaces from the Eikonal equation solution to form the inner and outer mesh boundaries. The mesh domain is then enclosed by interpolating between the edges of the inner and outer bounding surfaces. The interior mesh can then be formed through bi-linear interpolation methods, such as blending functions (Liseikin, 2004; Shragge, 2006).

Figure 4c presents the corresponding singularity-free mesh. The grid is regularly-spaced on the outer isochron and has dimples at the locations of removed singularities. These discontinuities have been reduced by applying a smoothing operator to the Eikonal equation solution before calculating the mesh. Importantly, coordinate mesh smoothing usually does not affect propagation accuracy because the coordinate system mesh forms only the skeleton on which wavefield extrapolation occurs. However, for meshes exhibiting rough and/or discontinuous boundaries, even excessive local smoothing cannot generate coefficients that are smooth enough to be accurately represented with standard extrapolation techniques.

2D Green's Function Generation

The third test uses RWE to model 2D Green's functions on coordinate systems constructed by the aforementioned approach. Figure 5 presents a slice through the SEG-EAGE salt velocity model used for the test. Importantly, the contrast between the salt body and sediment velocities leads to complicated wavefield propagation including triplication and multipathing. Figure 5a shows the velocity model with an overlain coordinate system generated by meshing procedure discussed in the section above. The velocity model in the RWE domain is illustrated Figure 5b.

Figure 5c shows the impulse response tests in the RWE domain. The impulses conform

fairly well to the travel-time steps, except where they enter the salt body in the lower left of the image. The migration results mapped back to Cartesian space are shown in Figure 5d. The complicated wavefield to the left of the shot point advances through the salt body and subsequently refracts upward. Note also the presence of wide-angle reflections from the top-salt/sediment interface. Figure 6 presents a comparison test between two-way finite-difference, RWE and Cartesian extrapolation. The three wavefields are fairly similar beneath and to the right of the shot-point except for a 90° phase-change associated with differences between modeling the finite difference and Cartesian point-source (Figures 6a and 6c) versus the RWE plane-wave (Figure 6b). However, significant differences are noted to the left of the shot-point. The upper two panels contain strong reflections from the salt-sediment that are fairly well matched in location. Cartesian-based extrapolation, though, propagates wavefields laterally neither with the same accuracy nor upward at all. Hence, this energy is absent from the propagating wavefield in the lower panel.

Differences in the modeled amplitudes at and above the salt interface in the upper two panels are attributed to differences between finite difference and one-way wavefield extrapolation implementations. Finite differences better models amplitudes in the presence of velocity gradients in the propagation direction. Thus, incident energy is more accurately partitioned at the top sediment-salt interface leading to the lower amplitudes of subsalt multi-pathed arrivals. The RWE wavefield underestimates the reflection contribution and allows significantly more energy to be transmitted into and through the salt body. This modeling inaccuracy leads to the more pronounced multipathing in the RWE panel below the salt body and the more complicated wavefield behavior relative to the Cartesian wavefield example. However, incorporating higher-order terms (Zhang et al., 2003) into the RWE formalism would likely diminish the differences between the finite difference and RWE

results.

3D Point Source Coordinates

The procedure discussed above can be extended to 3D point-source coordinate systems. However, any wavefield extrapolation procedure in near-spherical coordinates must account for the apparent singularity at the poles (i.e. vertically downward). This requires appropriately discritizing the spherical shell making up an extrapolation step in the presence of an ever diminishing solid angle toward the polar regions. One approach is to rotate the poles such that the small arc-length regions are at the surface rather than vertically downward (Schneider, 1995). A second approach is to simply avoid sampling at the existing polar singularity (Fowler, 1995). Both solutions, though, have highly variable spatial sampling because regular spherical angle discritization leads to highly variable sampling in Cartesian space.

Another solution is to choose a spherical shell discritization that has a fairly uniform distribution in the Cartesian domain. Herein, I use a 3D point source gridding technique based on the Winkel-Tripel cartographic projection (Bugayevskiy and Snyder, 1995). Figure 7 illustrates this projection for a constant spherical surface. Note that the mapping does not eliminate distortions in area, direction or distance; rather, it minimizes the sum of all three.

A 3D point-source coordinate system can be constructed by using a set of concentric shells with spherical Winkel-Tripel gridding of increasing radii (or equally by the Eikonal equation solution method described above). This results in the following analytic 3D point-

source coordinate system:

$$
\begin{aligned}
x_1 &= \xi_3(2\xi_1/\pi + 2\,w\,\alpha\cos\xi_2\sin(\xi_1/2))/2 \\
x_2 &= \xi_3(\xi_2 + 2\,w, \alpha\sin\xi_2)/2 \\
x_3 &= \sqrt{\xi_3^2 - x_1^2 - x_2^2}
\end{aligned}
\tag{29}
$$

where ξ_3 is in the radial direction, ξ_1 and ξ_2 are latitude parallels and longitude meridians, respectively, and,

$$
\begin{aligned}
\alpha &= \cos^{-1}\left(\cos\xi_2\cos(\xi_1/2)\right) \\
w &= \begin{cases} 0, & \sin\alpha = 0 \\ (\sin\alpha)^{-1}, & \text{otherwise} \end{cases}
\end{aligned}
\tag{30}
$$

Wavefield extrapolation is performed by stepping a point-source wavefield outward in the radial direction ξ_3.

Figure 8 presents an example of a wavefield extrapolated on 3D point source coordinate mesh (Figure 8a) and, for comparison, on a Cartesian grid (Figure 8b). The 3D test example uses the Elf-IFP-CGG synthetic velocity model generated from field data observations from North Sea Block L7d. The sediments located beneath the shot point form a mostly v(z) profile, while the salt body to the left creates a more complex geologic setting. Overlain are a number of impulse responses associated with different travel times. Note that the RWE approach models turning waves to the left of the shot point, whereas Cartesian propagation cannot by design. However, because the coordinate system does not cover the full velocity field, boundary artifacts are present within the RWE propagation domain and need to be suppressed. Overall, though, the extrapolation result demonstrates the stability of wavefield propagation on 3D Winkel-Tripel meshes and an improved accuracy over one-way propagators onssss 3D Cartesian grids.

IMPLEMENTATION COSTS

The introduction of additional mixed-domain coefficients into the dispersion relationship leads to both increased computation costs and memory requirements. To give an example of the cost overhead of the RWE approach, relative to Cartesian, the algorithm was benchmarked on the 2D computational grid (512x512 samples) used to generate Figure 6. Tests were conducted on two codes that differed only in the phase-shift and split-step Fourier subroutines. The RWE code implemented the 2D non-orthogonal extrapolation operator in equation C-9, while the Cartesian implementation used the regular expression (i.e. $g_{33} = g_{11} = 1$ and $g_{13} = n_3 = 0$ in equation C-9).

Table 1 presents the results of the benchmark test. A total of 82 frequencies were propagated a total of 511 extrapolation steps requiring 41 092 calls to the SSF operator. The tests involved 112 996 calls to the phase-shift routine, or almost three per extrapolation step as this number varied according toss velocity model complexity. The most significant observation is that the RWE algorithm is roughly 1.35 times slower than the equivalent Cartesian code. Most of the overhead occurs in the phase-shift and SSF subroutines that are roughly 2.25 and 2.0 times slower, respectively. Whether these costs may be reduced by implementing look-up tables remains an unresolved question. An additional computational overhead is the time required to calculate the geometrical factors a_i in equation 10. This cost, though, can usually be spread over the total number of shots for stationary geometries. Furthermore, the extra cost of non-orthogonal propagation, relative to that on semi-orthogonal mesh, is $<5\%$ since this affects only phase-shift operation and occurs outside of the more costly square-root calculation.

A second major implementation issue is the memory required to store the non-stationary

a_i coefficients. Holding each additional coefficient in core requires allocating memory equivalent to a velocity model, which can become the limiting issue for large 3D models. (For example, a 3D non-orthogonal grid requires an additional 20% memory to store coefficients relative to a semi-orthogonal mesh.) Unfortunately, the alternatives to allocating memory, recalculating the a_i coefficients locally each time or reading them from disk, are inefficient. An alternate approach is to consider analytic coordinate systems (Shragge and Shan, 2007) similar to those found in Figures 2 and 3. Their main advantage is that they result in analytically defined extrapolation operators that avoid most problems associated with additional computational and memory overhead costs. Further discussion on this point, however, is beyond the scope of this paper.

CONCLUDING REMARKS

This paper addresses existing issues with Riemannian wavefield extrapolation theory by extending RWE to smoother, but non-orthogonal, coordinate systems. The paper demonstrates that one can generate an acoustic wave equation in general 3D Riemannian spaces, and that the corresponding extrapolation wavenumber decouples from the other wavenumbers. This wavenumber can then be incorporated into a one-way wavefield extrapolation operator appropriate for propagating wavefields. An approximate PSPI plus multi-coefficient SSF solution of the one-way wavefield extrapolation operator is then derived. A method for generating computational meshes that are unconditionally singularity-free is detailed, and used to generate examples that illustrate wavefield propagation on non-orthogonal coordinate meshes using RWE operators. Accordingly, this opens up a range of imaging possibilities including Riemannian plane-wave migration in elliptical polar coordinates.

ACKNOWLEDGMENTS

I acknowledge the contributions of Paul Sava and Sergey Fomel in laying the groundwork for the current theory and for ongoing RWE conversations, and I thank Biondo Biondi, Bob Clapp, Brad Artman, Paul Fowler, Tom Dickens, and Peter Traynin for enlightening discussions. I also acknowledge the reviewers of this manuscript reviewer and thank them for their helpful comments. The sponsors of the SEP consortium provided funding for this work.

REFERENCES

Albertin, U., D. Yingst, and H. Jaramillo, 2001, Comparing common-offset Maslov, Gaussian beam, and coherent state migrations: 71st Ann. Internat. Mtg., Expanded Abstracts, 913–916, Soc. of Expl. Geophys.

Brandsberg-Dahl, S. and J. Etgen, 2003, Beam-wave imaging, *in* Expanded Abstracts, 977–980, Soc. of Expl. Geophys.

Bugayevskiy, L. M. and J. P. Snyder, 1995, Map projections - A Reference Manual: Taylor & Francis Inc., Philadelphia, PA.

Claerbout, J., 1985, Imaging the Earth's Interior: Stanford University.

Etgen, J., 2002, Waves, beams and Dimensions: An illuminating if incoherent view of the future of migration, *in* invited presentation, Soc. of Expl. Geophys.

Fowler, P. J., 1995, Finite-difference solutions of the 3-D Eikonal equation in spherical coordinates: Presented at the 65^{th} Annual SEG Convention.

Gazdag, J., 1978, Wave equation migration with the phase-shift method: Geophysics, **43**, 1342–1351.

Guggenheimer, H., 1977, Differential Geometry: Dover Publications, Inc., New York.

Hale, D., N. Hill, and J. Stephani, 1992, Imaging salt with turning seismic waves: Geophysics, **57**, 1453–1462.

Hill, N. R., 2001, Prestack Gaussian-beam depth migration: Geophysics, **66**, 1240–1250.

Liseikin, V., 2004, A Computational Differential Geometry Approach to Grid Generation: Springer-Verlag, Berlin.

Nichols, D., 1994, Imaging complex structures using band-limited Green's functions: Ph.D. thesis, Stanford University.

Sava, P. C. and S. Fomel, 2001, 3-D traveltime computation using Huygens wavefront

tracing: Geophysics, **66**, 883–889.

———, 2005, Riemannian wavefield extrapolation: Geophysics, **70**, T45–T56.

Schneider, W. A., 1995, Robust and efficient upwind finite-difference traveltime calculations in three dimensions: Geophysics, **60**, 1108–1117.

Shragge, J., 2006, Differential mesh generation: Soc. of Expl. Geophys., Expanded Abstracts, 2206–2209.

Shragge, J. and P. Sava, 2005, Wave-equation migration from topography, *in* Expanded Abstracts, 1842–1845, Soc. of Expl. Geophys.

Shragge, J. and G. Shan, 2007, Prestack depth migration in elliptic coordinates: Presented at the Soc. of Expl. Geophys.

Stoffa, P. L., J. T. Fokkema, R. M. de Luna Freire, and W. P. Kessinger, 1990, Split-step Fourier migration: Geophysics, **55**, 410–421.

Synge, J. L. and A. Schild, 1949, Tensor Calculus: University of Toronto Press.

Tang, Y. and R. Clapp, 2006, Selection of reference-anisotropy parameters for wavefield extrapolation by Lloyd's algorithm: Soc. of Expl. Geophys., Expanded Abstracts, 189–192.

Zhang, Y., S. Xu, and G. Zhang, 2006, Imaging complex salt bodies with turning-wave one-way wave-equation, *in* Expanded Abstracts, Soc. of Expl. Geophys.

Zhang, Y., G. Zhang, and N. Bleistein, 2003, True amplitude wave equation migration arising from true amplitude one-way wave equations: Inverse Problems, **19**, 1113–1138.

APPENDIX A

Geometry in a generalized 3D Riemannian space is described by a symmetric metric tensor, $g_{ij} = g_{ji}$, that relates the geometry in a general non-orthogonal coordinate system, $\{\xi_1, \xi_2, \xi_3\}$, to an underlying Cartesian mesh, $\{x_1, x_2, x_3\}$ (Guggenheimer, 1977). In matrix form, the metric tensor is written,

$$[g_{ij}] = \begin{bmatrix} g_{11} & g_{12} & g_{13} \\ g_{21} & g_{22} & g_{23} \\ g_{31} & g_{32} & g_{33} \end{bmatrix} = \begin{bmatrix} g_{11} & g_{12} & g_{13} \\ g_{12} & g_{22} & g_{23} \\ g_{13} & g_{23} & g_{33} \end{bmatrix}, \tag{A-1}$$

where g_{11}, g_{12}, g_{22}, g_{13}, g_{23} and g_{33} are functions linking the two coordinate systems through,

$$\begin{aligned} g_{11} &= \frac{\partial x_k}{\partial \xi_1}\frac{\partial x_k}{\partial \xi_1}, \quad g_{12} = \frac{\partial x_k}{\partial \xi_1}\frac{\partial x_k}{\partial \xi_2}, \quad g_{22} = \frac{\partial x_k}{\partial \xi_2}\frac{\partial x_k}{\partial \xi_2}, \\ g_{13} &= \frac{\partial x_k}{\partial \xi_1}\frac{\partial x_k}{\partial \xi_3}, \quad g_{23} = \frac{\partial x_k}{\partial \xi_2}\frac{\partial x_k}{\partial \xi_3}, \quad g_{33} = \frac{\partial x_k}{\partial \xi_3}\frac{\partial x_k}{\partial \xi_3}. \end{aligned} \tag{A-2}$$

The associated (or inverse) metric tensor, g^{ij}, is given by,

$$\left[g^{ij}\right] = \frac{1}{|\mathbf{g}|}\begin{bmatrix} g_{22}g_{33} - g_{23}^2 & g_{13}g_{23} - g_{12}g_{33} & g_{12}g_{23} - g_{13}g_{22} \\ g_{13}g_{23} - g_{12}g_{33} & g_{11}g_{33} - g_{13}^2 & g_{12}g_{13} - g_{11}g_{23} \\ g_{12}g_{23} - g_{13}g_{22} & g_{12}g_{13} - g_{11}g_{23} & g_{11}g_{22} - g_{12}^2 \end{bmatrix}, \tag{A-3}$$

and has the following metric discriminant, $|\mathbf{g}|$,

$$|\mathbf{g}| = g_{11}g_{22}g_{33} - g_{12}^2 g_{33} - g_{23}^2 g_{11} - g_{13}^2 g_{22} + 2g_{12}g_{13}g_{23} \tag{A-4}$$

A weighted metric tensor, $m^{ij} = \sqrt{|\mathbf{g}|}\, g^{ij}$, is also used throughout the paper.

APPENDIX B

The extrapolation wavenumber defined in equations 10 and 11 cannot generally be implemented exactly in the Fourier domain due to a simultaneous spatial dependence (i.e. a function of both ξ_1 and k_{ξ_1}). This can be addressed using an multi-coefficient version of the split-step Fourier approximation (Stoffa et al., 1990) that uses Taylor expansions to separate k_{ξ_3} into two parts: $k_{\xi_3} \approx k_{\xi_3}^{PS} + k_{\xi_3}^{SSF}$. Wavenumbers $k_{\xi_3}^{PS}$ and $k_{\xi_3}^{SSF}$ represent a pure Fourier $(\omega - \mathbf{k}_\xi)$ domain phase-shift and a mixed $(\omega - \xi)$ domain split-step correction, respectively.

The phase-shift term is given by,

$$k_{\xi_3}^{PS} = -b_1 k_{\xi_1} - b_2 k_{\xi_2} + \mathrm{i}b_3 \pm \left[b_4^2 \omega^2 - b_5^2 k_{\xi_1}^2 - b_6^2 k_{\xi_2}^2 - b_7 k_{\xi_1} k_{\xi_2} + \mathrm{i}b_8\, k_{\xi_1} + \mathrm{i}b_9\, k_{\xi_2} - b_{10}^2 \right]^{\frac{1}{2}}, \tag{B-1}$$

where $b_i = b_i(\xi_3)$ are reference values of $a_i = a_i(\xi_1, \xi_2, \xi_3)$. The split-step approximation is developed by performing a Taylor expansion about each coefficient a_i and evaluating the results at stationary reference values b_i. Assuming that the stationary values of k_{ξ_1} and k_{ξ_2} are zero, the split-step correction i as follows,

$$k_{\xi_3}^{SSF} = \left.\frac{\partial k_{\xi_3}}{\partial a_3}\right|_0 (a_3 - b_3) + \left.\frac{\partial k_{\xi_3}}{\partial a_4}\right|_0 (a_4 - b_4) + \left.\frac{\partial k_{\xi_3}}{\partial a_{10}}\right|_0 (a_{10} - b_{10}), \tag{B-2}$$

where "0" denotes "with respect to a reference medium". The partial differential expressions in equation B-2 are,

$$\left.\frac{\partial k_{\xi_3}}{\partial a_3}\right|_0 = b_3, \qquad \left.\frac{\partial k_{\xi_3}}{\partial a_4}\right|_0 = \frac{b_4\, \omega^2}{\sqrt{b_4^2\, \omega^2 - b_{10}^2}}, \qquad \left.\frac{\partial k_{\xi_3}}{\partial a_{10}}\right|_0 = -\frac{b_{10}}{\sqrt{b_{10}^2\, \omega^2 - b_{10}^2}}, \tag{B-3}$$

resulting in the following split-step Fourier correction wavenumber,

$$k_{\xi_3}^{SSF} = \mathrm{i}\, b_3\ (a_3 - b_3) + \frac{b_4\, \omega^2\ (a_4 - b_4)}{\sqrt{b_4^2\, \omega^2 - b_{10}^2}} - \frac{b_{10}\ (a_{10} - b_{10})}{\sqrt{b_4\, \omega^2 - b_{10}^2}}. \tag{B-4}$$

APPENDIX C

The extrapolation wavenumber developed in equation 10 is appropriate for any non-orthogonal Riemannian geometry. However, there are a number of situations where symmetry or partial orthogonality are present. Moreover, kinematic approximations can be made where one ignores all imaginary wavenumber components. This Appendix discusses these situations.

3D Semi-orthogonal Coordinate Systems - Semi-orthogonal coordinate systems occur where one coordinate (ξ_3) is orthogonal to the other two coordinates (ξ_1 and ξ_2) (Sava and Fomel, 2005). In these cases the m^{13} and m^{23} components of the weighted metric tensor are identically zero, which leads to the following extrapolation wavenumber,

$$k_{\xi_3} = \mathrm{i}a_3 \pm \left[a_4^2\omega^2 - a_5^2 k_{\xi_1}^2 - a_6^2 k_{\xi_2}^2 - a_7 k_{\xi_1} k_{\xi_2} + \mathrm{i}a_8 k_{\xi_1} + \mathrm{i}a_9 k_{\xi_2} - a_{10}^2\right]^{\frac{1}{2}}, \tag{C-1}$$

where,

$$\mathbf{a} = \left[0 \quad 0 \quad \frac{n^3}{2m^{33}} \quad \frac{s}{\sqrt{g^{33}}} \quad \sqrt{\frac{g^{11}}{g^{33}}} \quad \sqrt{\frac{g^{22}}{g^{33}}} \quad \frac{2g^{12}}{g^{33}} \quad \frac{n^1}{m^{33}} \quad \frac{n^2}{m^{33}} \quad \frac{n^3}{2m^{33}}\right]^{\mathbf{T}}. \tag{C-2}$$

which are identical to the coefficients recovered by Sava and Fomel (2005).

3D Kinematic Coordinate Systems - Wave-equation migration amplitudes are generally inexact in laterally variant media - even in Cartesian-based systems. Hence, one beneficial approximation that reduces computational cost is to consider only the kinematic terms in equation 10. This approximate generates the following extrapolation wavenumber,

$$\hat{k_{\xi_3}} = -a_1 k_{\xi_1} - a_2 k_{\xi_2} \pm \left[a_4^2\omega^2 - a_5^2 k_{\xi_1}^2 - a_6^2 k_{\xi_2}^2 - a_7 k_{\xi_1} k_{\xi_2} - a_{10}^2\right]^{\frac{1}{2}}, \tag{C-3}$$

where,

$$\mathbf{a} = \left[\frac{g^{13}}{g^{33}} \quad \frac{g^{23}}{g^{33}} \quad 0 \quad \frac{s}{\sqrt{g^{33}}} \quad \sqrt{\frac{g^{11}}{g^{33}} - \left(\frac{g^{13}}{g^{33}}\right)^2} \quad \sqrt{\frac{g^{22}}{g^{33}} - \left(\frac{g^{23}}{g^{33}}\right)^2} \quad \frac{2\,g^{12}}{g^{33}} - \frac{2\,g^{13}g^{23}}{(g^{33})^2} \quad 0 \quad 0 \quad \frac{n^3}{2m^{33}} \right]^{\mathbf{T}}. \tag{C-4}$$

3D Kinematic Semi-orthogonal coordinate systems - Combining the two above restrictions yields the following extrapolation wavenumber,

$$\hat{k_{\xi_3}} = \pm \left[a_4^2\omega^2 - a_5^2 k_{\xi_1}^2 - a_6^2 k_{\xi_2}^2 - a_7 k_{\xi_1} k_{\xi_2} - a_{10}^2 \right]^{\frac{1}{2}}, \tag{C-5}$$

where,

$$\mathbf{a} = \left[0 \quad 0 \quad 0 \quad \frac{s}{\sqrt{g^{33}}} \quad \sqrt{\frac{g^{11}}{g^{33}}} \quad \sqrt{\frac{g^{22}}{g^{33}}} \quad \frac{2\,g^{12}}{g^{33}} \quad 0 \quad 0 \quad \frac{n^3}{2m^{33}} \right]^{\mathbf{T}}. \tag{C-6}$$

2D Non-orthogonal coordinate systems - Two-dimensional situations are handled by identifying $\xi_2 = 0$. All derivatives in the associated metric tensor g^{ij} with respect coordinate ξ_2 are identically zero, and the resulting 2D non-orthogonal coordinate system wavenumber is,

$$k_{\xi_3} = -a_1 k_{\xi_1} + \mathrm{i}a_3 \pm \left[a_4^2\omega^2 - a_5^2 k_{\xi_1}^2 + \mathrm{i}a_8 k_{\xi_1} - a_{10}^2 \right]^{\frac{1}{2}}, \tag{C-7}$$

where,

$$\mathbf{a} = \left[\frac{g^{13}}{g^{33}} \quad 0 \quad \frac{n^3}{2m^{33}} \quad \frac{s}{\sqrt{g^{33}}} \quad \sqrt{\frac{g^{11}}{g^{33}} - \left(\frac{g^{13}}{g^{33}}\right)^2} \quad 0 \quad 0 \quad \frac{n^1}{m^{33}} - \frac{m^{13}n^3}{(m^{33})^2} \quad 0 \quad \frac{n^3}{2m^{33}} \right]^{\mathbf{T}}. \tag{C-8}$$

2D Non-orthogonal Kinematic Coordinate Systems - Two-dimensional kinematic situations are handled through identity $\xi_2 = 0$. Again, all derivatives in the associated metric tensor g^{ij} with respect coordinate ξ_2 are identically zero, and the 2D non-orthogonal kinematic extrapolation wavenumber is

$$\hat{k_{\xi_3}} = -a_1 k_{\xi_1} \pm \left[a_4^2\omega^2 - a_5^2 k_{\xi_1}^2 - a_{10}^2 \right]^{\frac{1}{2}}, \tag{C-9}$$

where,

$$\mathbf{a} = \left[\frac{g^{13}}{g^{33}} \quad 0 \quad 0 \quad \frac{s}{\sqrt{g^{33}}} \quad \sqrt{\frac{g^{11}}{g^{33}} - \left(\frac{g^{13}}{g^{33}}\right)^2} \quad 0 \quad 0 \quad 0 \quad 0 \quad \frac{n^3}{2m^{33}} \right]^{\mathbf{T}}. \tag{C-10}$$

2D Orthogonal Coordinate Systems - Two-dimensional situations are handled with $\xi_2 = g_{13} = 0$. Accordingly, all derivatives in the associated metric tensor g^{ij} with respect coordinate ξ_2 are identically zero, and the 2D orthogonal coordinate system is represented by

$$k_{\xi_3} = ia_3 \pm \left[a_4^2\omega^2 - a_5^2 k_{\xi_1}^2 + \mathrm{i}a_8 k_{\xi_1} - a_{10}^2 \right]^{\frac{1}{2}}, \tag{C-11}$$

where,

$$\mathbf{a} = \left[0 \quad 0 \quad \frac{n_3}{2m^{33}} \quad \frac{s}{\sqrt{g^{33}}} \quad \sqrt{\frac{g^{11}}{g^{33}}} \quad 0 \quad 0 \quad \frac{n^1}{m^{33}} \quad 0 \quad \frac{n^3}{2m^{33}} \right]^{\mathbf{T}}. \tag{C-12}$$

2D Orthogonal Kinematic Coordinate Systems - The above two approximations can be combined to yield the following extrapolation wavenumber for 2D orthogonal kinematic coordinate systems,

$$\hat{k_{\xi_3}} = \pm \left[a_4^2\omega^2 - a_5^2 k_{\xi_1}^2 - a_{10}^2 \right]^{\frac{1}{2}}, \tag{C-13}$$

where,

$$\mathbf{a} = \left[0 \quad 0 \quad 0 \quad \frac{s}{\sqrt{g^{33}}} \quad \sqrt{\frac{g^{11}}{g^{33}}} \quad 0 \quad 0 \quad 0 \quad 0 \quad \frac{n^3}{2m^{33}} \right]^{\mathbf{T}}. \tag{C-14}$$

Extrapolation Type	Operation	Number of Calls	Total Time (s)	Time per Frequency (s)
RWE	Frequency Loop	82	55.4	0.676
RWE	Split-step Fourier	41092	4.2	0.051
RWE	Phase-shift	112996	17.1	0.209
RWE	Interpolation	112996	4.6	0.056
Cart	Frequency Loop	82	40.9	0.499
Cart	Split-step Fourier	41092	2.1	0.026
Cart	Phase-shift	112996	7.6	0.093
Cart	Interpolation	112996	4.4	0.054

Table 1: Comparison of computational costs of the split-step Fourier and phase-shift subroutines for the RWE and equivalent Cartesian implementations. Test results cited here were for calculating the 2D example shown in Figure 6.

LIST OF FIGURES

1 Illustration of problems with semi-orthgonal RWE computational grids. a) Singularities in a coordinate system generated by ray-tracing that lead to zero-division in RWE. b) Grid bunching for a topographically conformal coordinate system that cause significant lateral variation in each extrapolation step.

2 Sheared Cartesian coordinate system test. a) Coordinate system shear angle and velocity are $\theta = 25^\circ$ and 1500 ms^{-1}, respectively. b) Zero-offset data consist of 4 flat plane-wave impulses at $t = 0.2, 0.4, 0.6$ and 0.8 s that are correctly imaged at depths $z = 300, 600, 900$, and 1200 m.

3 Ellipsoidal polar coordinate system test example. a) velocity function $v(z) = 1500 + 0.35\,z$ overlain by a polar ellipsoidal coordinate system defined by parameter $a = 1 + 0.2\,\xi_3 - 0.05\,\xi_3^2$. b) Velocity model mapped in the RWE domain. c) Imaged reflectors in RWE domain. d) RWE domain image mapped to a Cartesian mesh.

4 Example of singularity-free mesh generation. a) Velocity model with three Gaussian velocity perturbations. Overlain is a coordinate mesh generated from ray-tracing. Note the triplication to either side of the shot-point, as well as the spreading beneath the shot point. b) Velocity model overlain by isochrons of an Eikonal equation solution for same shot-point. c) Singularity-free computational mesh.

5 Example of wave-equation generated Green's functions on structured non-orthogonal mesh for a slice through the SEG-EAGE salt velocity model. a) Salt model in physical space with an overlain ray-based mesh. b) Velocity model in the RWE domain. c) Wavefield propagated in ray-coordinates through velocity model shown in panel b. d) Wavefield in panel c interpolated back to Cartesian space.

6 Comparison between three different extrapolation methods. a) Two-way finite-difference. b) Riemannian wavefield extrapolation. c) Cartesian wavefield extrapolation.

7 Starting surface for Winkel-Tripel projection of unit hemisphere. Note that the cells on the unit hemisphere surface have nearly consistent area indicating fairly uniform sampling, and that not all parts of the unit hemisphere are sampled with this approach. A 3D coordinate system is generated by constructing many concentric Winkel-Tripel spherical shells of increasing radii.

8 3D modeling example using the Elf-IFP-CGG synthetic velocity. a) RWE on Winkel-Tripel coordinate system. b) Cartesian wavefield extrapolation.

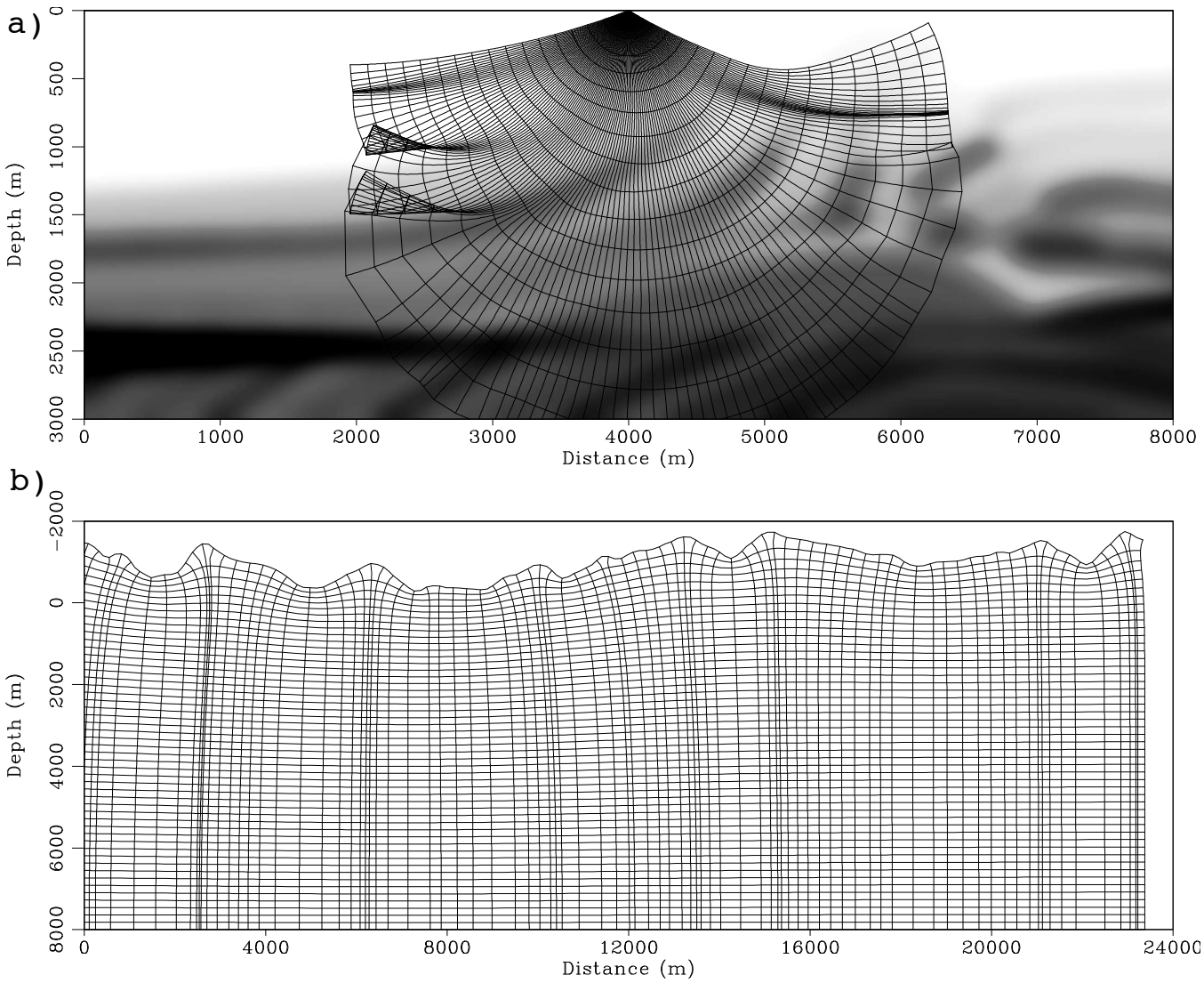

Figure 1: Illustration of problems with semi-orthgonal RWE computational grids. a) Singularities in a coordinate system generated by ray-tracing that lead to zero-division in RWE. b) Grid bunching for a topographically conformal coordinate system that cause significant lateral variation in each extrapolation step.

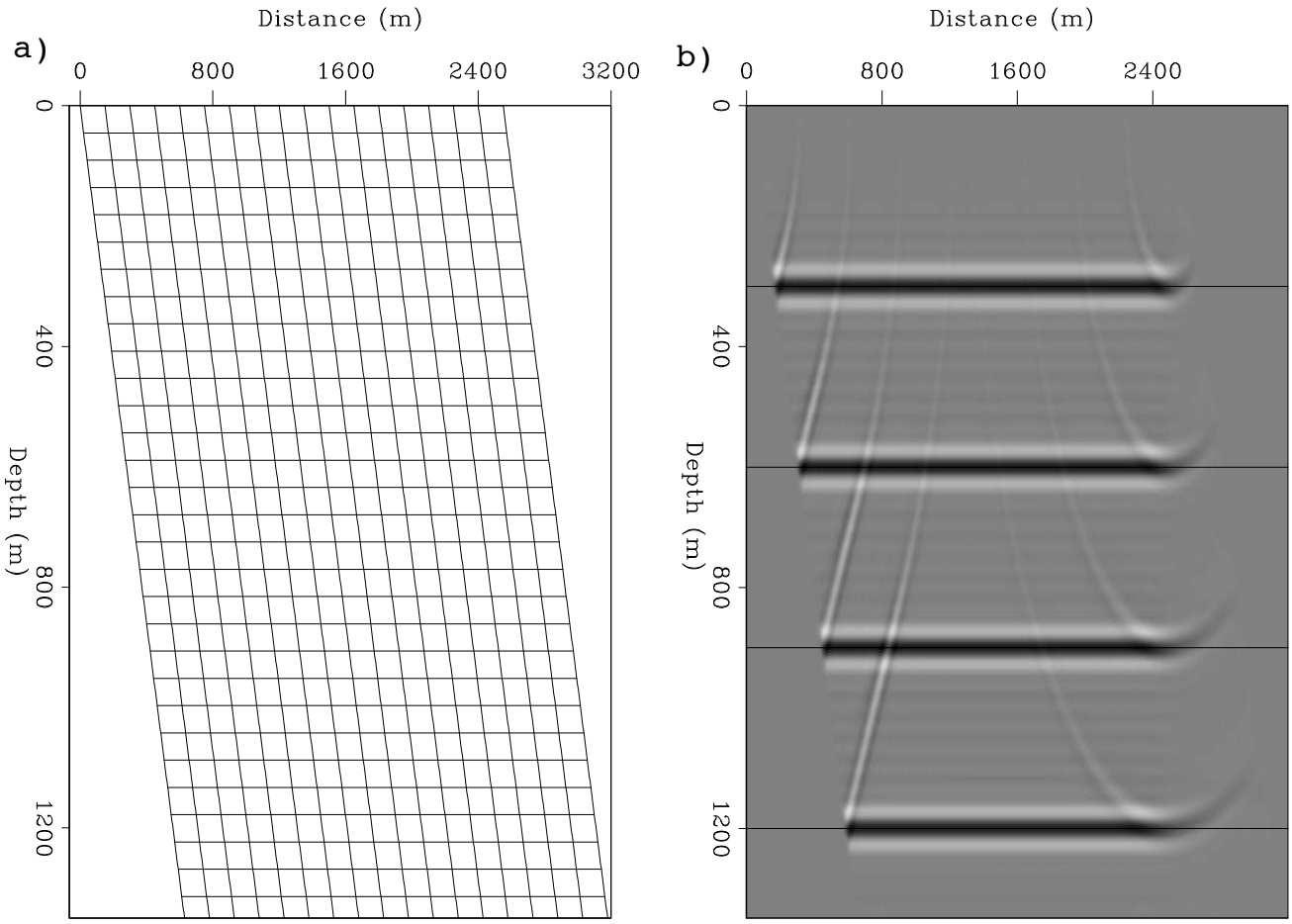

Figure 2: Sheared Cartesian coordinate system test. a) Coordinate system shear angle and velocity are $\theta = 25^\circ$ and 1500 ms^{-1}, respectively. b) Zero-offset data consist of 4 flat plane-wave impulses at $t = 0.2, 0.4, 0.6$ and 0.8 s that are correctly imaged at depths $z = 300, 600, 900$, and 1200 m.

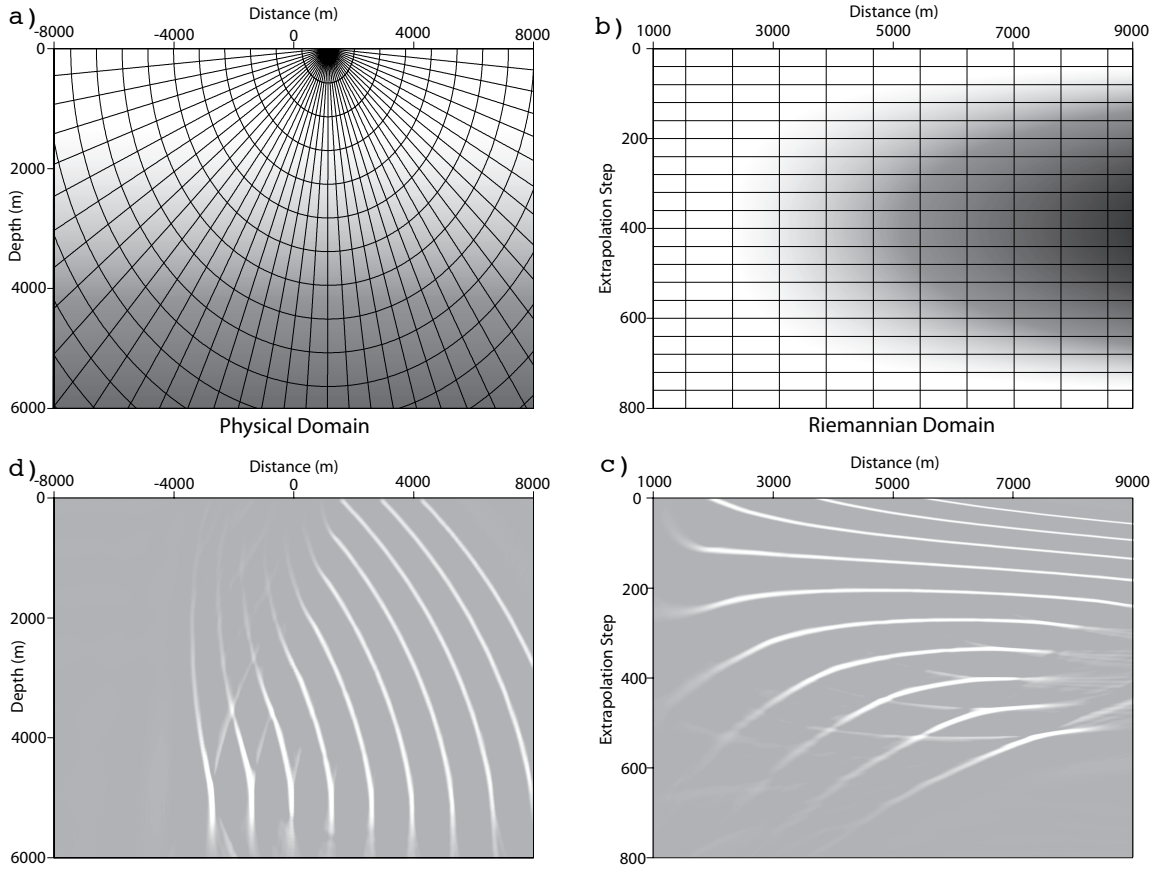

Figure 3: Ellipsoidal polar coordinate system test example. a) velocity function $v(z) = 1500 + 0.35\,z$ overlain by a polar ellipsoidal coordinate system defined by parameter $a = 1 + 0.2\,\xi_3 - 0.05\,\xi_3^2$. b) Velocity model mapped in the RWE domain. c) Imaged reflectors in RWE domain. d) RWE domain image mapped to a Cartesian mesh.

–

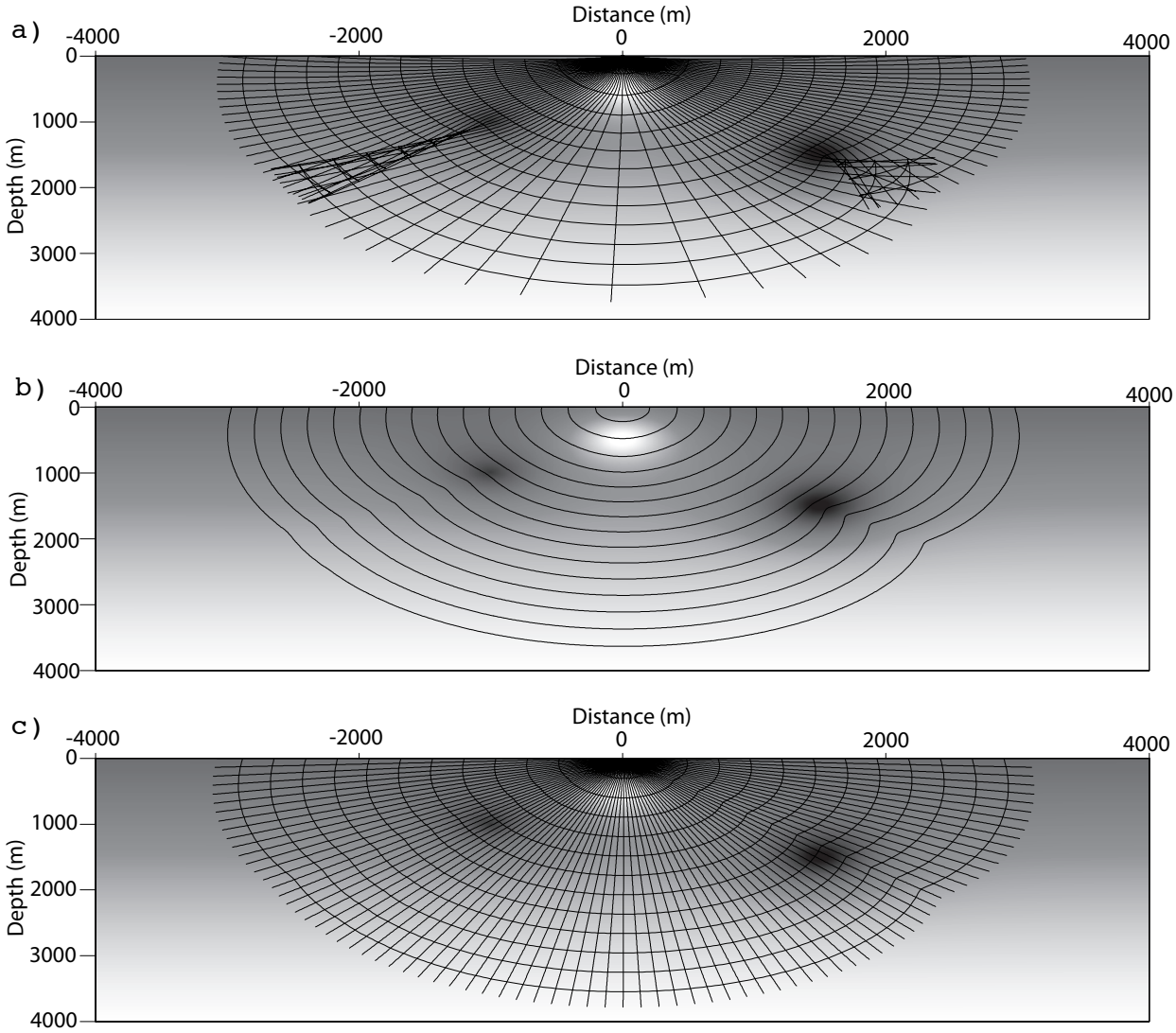

Figure 4: Example of singularity-free mesh generation. a) Velocity model with three Gaussian velocity perturbations. Overlain is a coordinate mesh generated from ray-tracing. Note the triplication to either side of the shot-point, as well as the spreading beneath the shot point. b) Velocity model overlain by isochrons of an Eikonal equation solution for same shot-point. c) Singularity-free computational mesh.

–

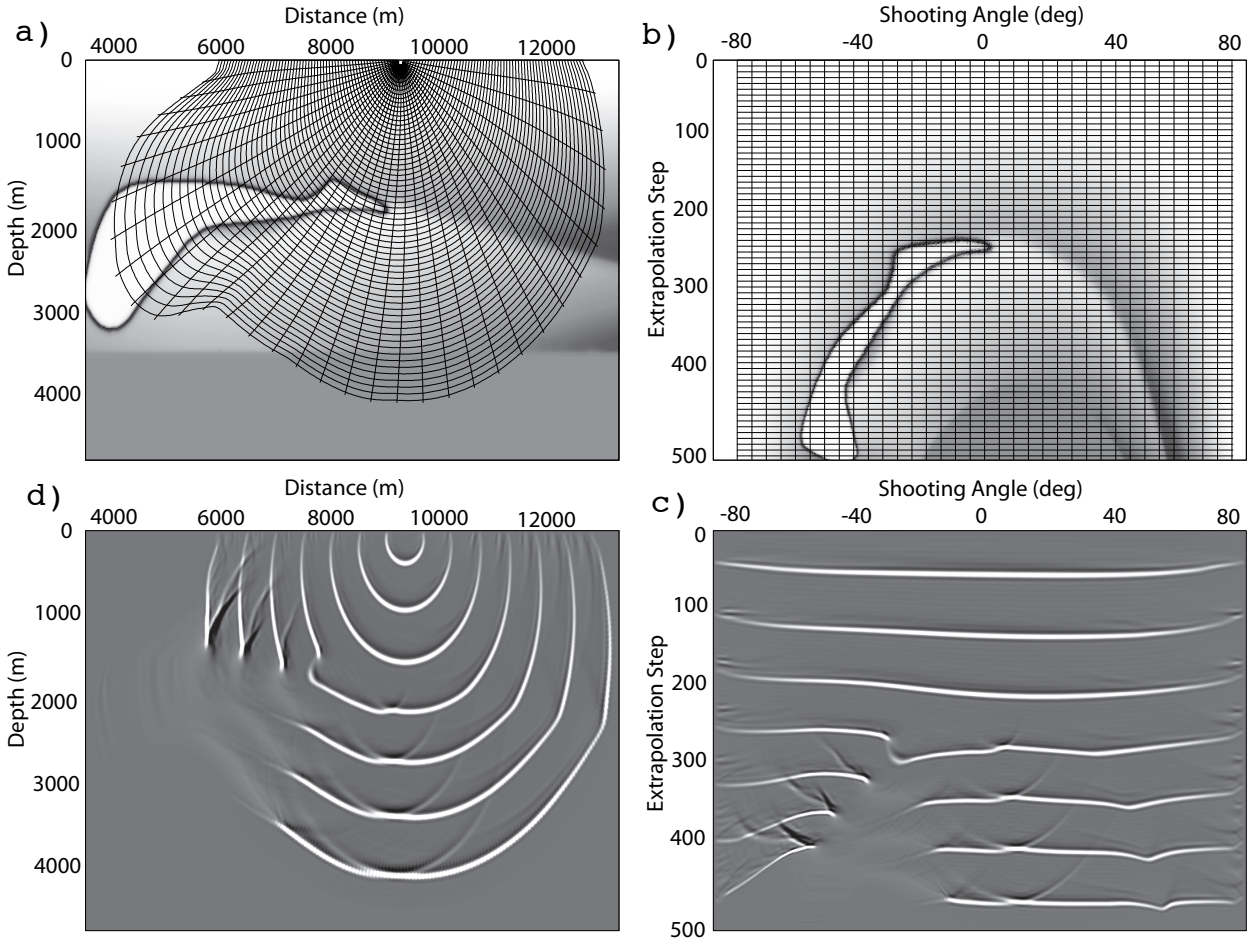

Figure 5: Example of wave-equation generated Green's functions on structured non-orthogonal mesh for a slice through the SEG-EAGE salt velocity model. a) Salt model in physical space with an overlain ray-based mesh. b) Velocity model in the RWE domain. c) Wavefield propagated in ray-coordinates through velocity model shown in panel b. d) Wavefield in panel c interpolated back to Cartesian space.

–

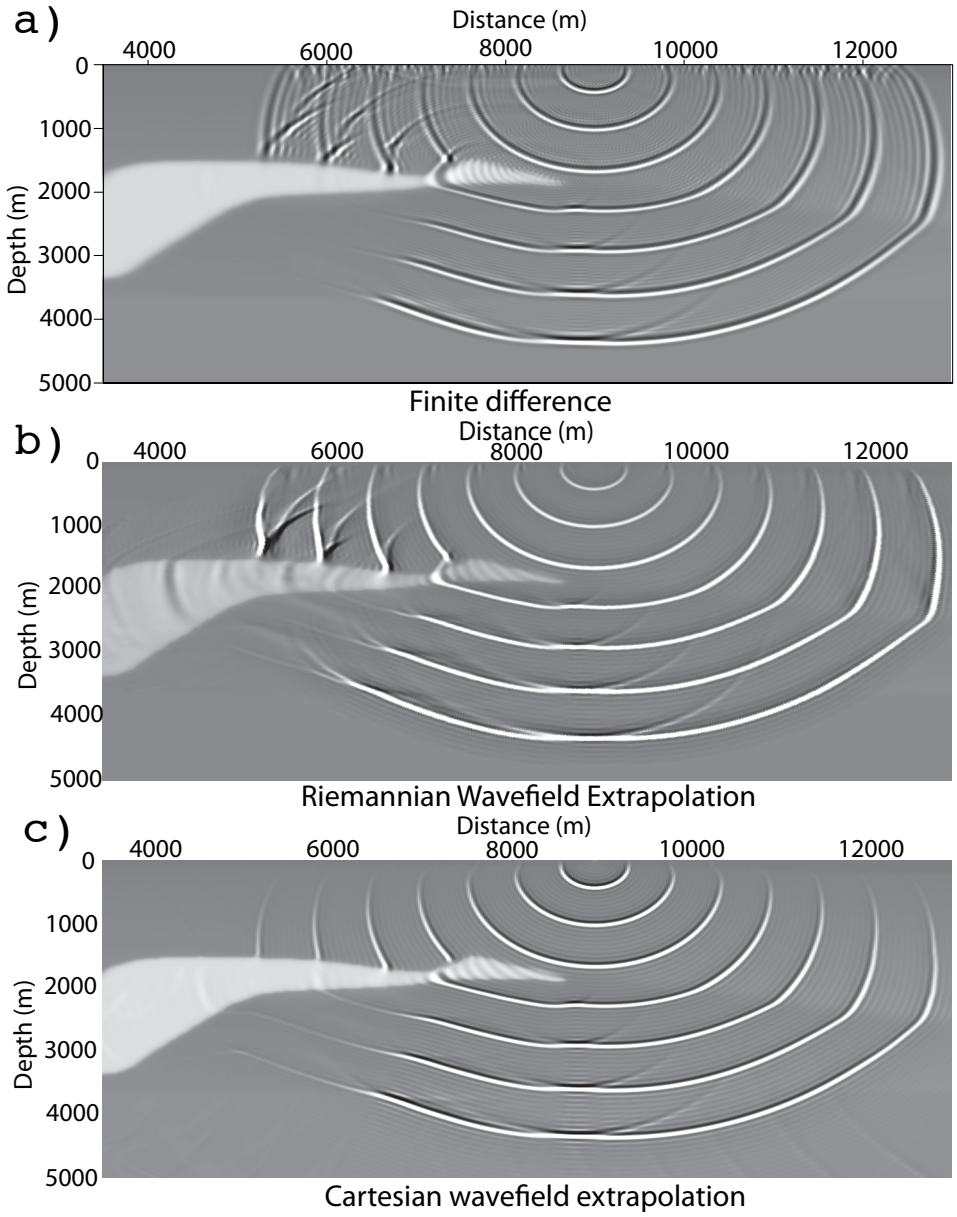

Figure 6: Comparison between three different extrapolation methods. a) Two-way finite-difference. b) Riemannian wavefield extrapolation. c) Cartesian wavefield extrapolation.

–

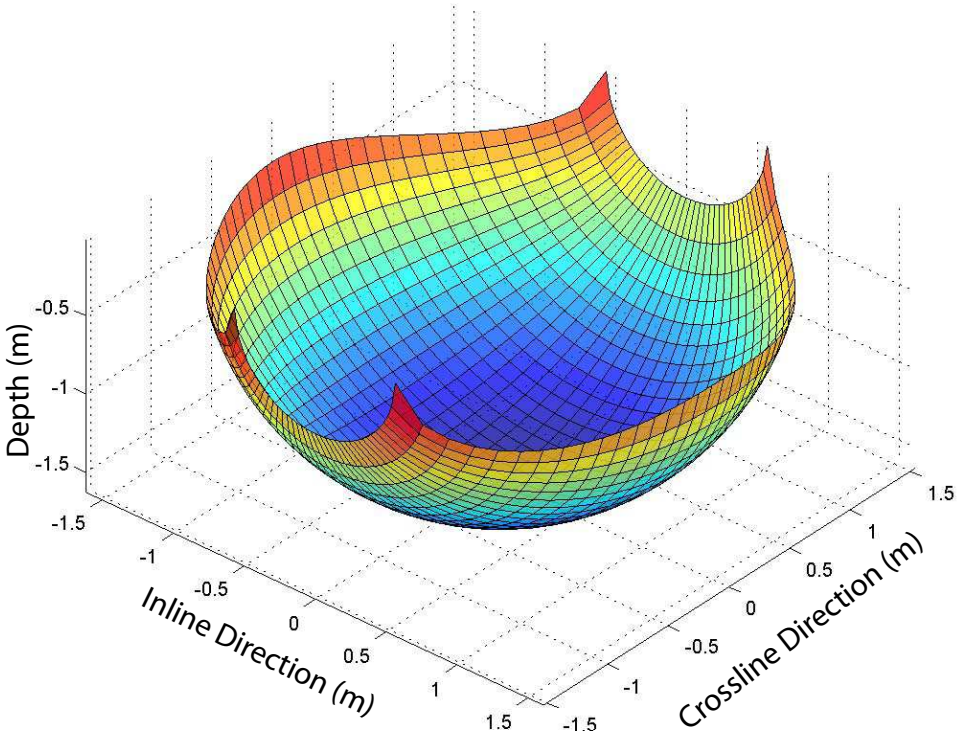

Figure 7: Starting surface for Winkel-Tripel projection of unit hemisphere. Note that the cells on the unit hemisphere surface have nearly consistent area indicating fairly uniform sampling, and that not all parts of the unit hemisphere are sampled with this approach. A 3D coordinate system is generated by constructing many concentric Winkel-Tripel spherical shells of increasing radii.

–

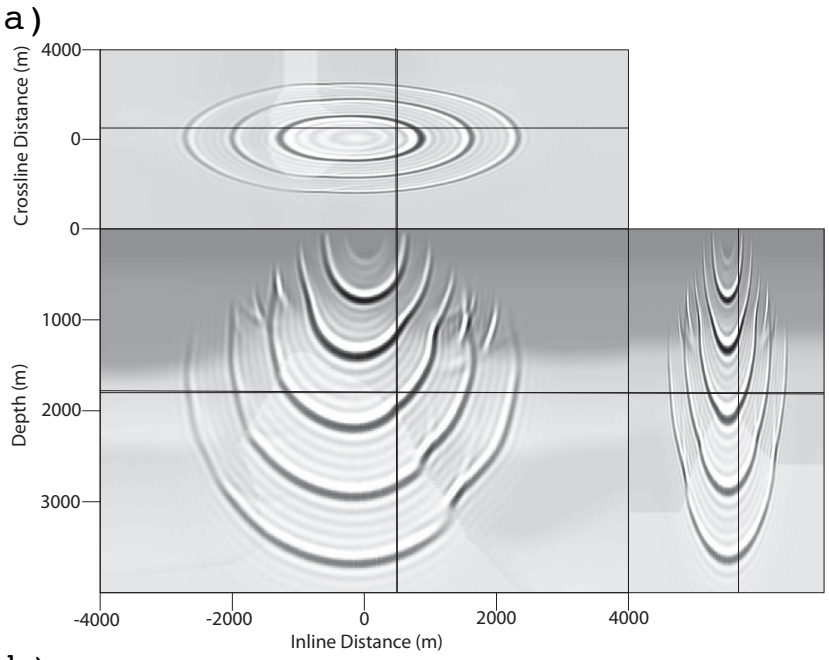

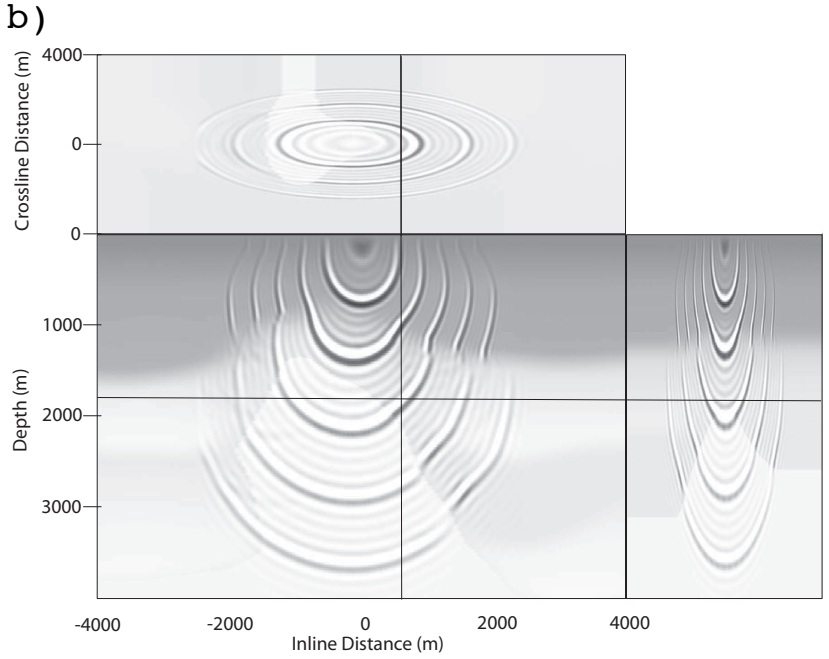

FIGURE 8

Figure 8: 3D modeling example using the Elf-IFP-CGG synthetic velocity. a) RWE on Winkel-Tripel coordinate system. b) Cartesian wavefield extrapolation.